Journal Pre-proof

Compositionally tunable Néel temperature in $Mn_{1-x}Co_xN$: A route to enhance magneto-ionic exchange bias control

Nicolau López-Pintó , Christopher J. Jensen , Zhijie Chen , Zihui Zeng , Christy J. Kinane , Andrew J. Caruana , Alexander J. Grutter , Julie A. Borchers , Enric Menéndez , Josep Nogués , Kai Liu , Jordi Sort

PII: S1005-0302(26)00252-5
DOI: https://doi.org/10.1016/j.jmst.2026.04.010
Reference: JMST 7573

To appear in: *Journal of Materials Science & Technology*

Received date: 20 October 2025
Revised date: 12 March 2026
Accepted date: 9 April 2026

Please cite this article as: Nicolau López-Pintó , Christopher J. Jensen , Zhijie Chen , Zihui Zeng , Christy J. Kinane , Andrew J. Caruana , Alexander J. Grutter , Julie A. Borchers , Enric Menéndez , Josep Nogués , Kai Liu , Jordi Sort , Compositionally tunable Néel temperature in $Mn_{1-x}Co_xN$: A route to enhance magneto-ionic exchange bias control, *Journal of Materials Science & Technology* (2026), doi: https://doi.org/10.1016/j.jmst.2026.04.010

Highlights

- Ternary Mn–Co–N antiferromagnetic compounds with tunable Néel temperature were developed.
- Voltage control of exchange bias and magnetization was achieved via magnetoionics.
- Nitrogen ion migration and diffusion pathways were elucidated using polarized neutron reflectometry.

Research Article

Compositionally tunable Néel temperature in $Mn_{1-x}Co_xN$: A route to enhance magneto-ionic exchange bias control

Nicolau López-Pintó [a, 1], Christopher J. Jensen [b, c, 1], Zhijie Chen [b, 1], Zihui Zeng [b], Christy J. Kinane [d], Andrew J. Caruana [d], Alexander J. Grutter [c], Julie A. Borchers [c], Enric Menéndez [a], Josep Nogués [e, f, *], Kai Liu [b, *], Jordi Sort [a, e, f, *]

[a] Departament de Física, Universitat Autònoma de Barcelona, 08193 Bellaterra (Cerdanyola del Vallès), Spain

[b] Physics Department, Georgetown University, Washington, DC 20057, USA

[c] NIST Center for Neutron Research, National Institute of Standards and Technology, Gaithersburg, MD 20899, USA

[d] ISIS Neutron Facility, STFC Rutherford Appleton Laboratory, Chilton, OX11 0QX, Oxfordshire, UK

[e] Catalan Institute of Nanoscience and Nanotechnology (ICN2), CSIC and BIST, Campus UAB, Bellaterra, 08193 Barcelona, Spain

[f] Institució Catalana de Recerca i Estudis Avançats (ICREA), Pg. Lluís Companys 23, 08010 Barcelona, Spain

[1] These authors contributed equally to this work.

[*] Corresponding authors.

E-mail addresses: josep.nogues@icn2.cat (J. Nogués); kai.liu@georgetown.edu (K. Liu); jordi.sort@uab.cat (J. Sort).

Keywords: Magneto-ionics; Exchange bias; MnCoN

Abstract

To address growing computational demands, energy-efficient hardware technologies such as

spintronics and neuromorphic computing have attracted significant interest. In particular, magneto-ionics offers a low-power, non-volatile approach to control magnetic properties, making it particularly suitable for manipulating antiferromagnetic (AFM) materials. In this work, we report magneto-ionic control of exchange bias (EB) in $Mn_{1-x}Co_xN$/Co with a compositionally tunable Néel temperature, T_N. The high T_N in MnN (> 650 K) typically necessitates high-temperature annealing, which triggers uncontrolled thermally induced ion-motion effects. Co addition to MnN reduces T_N, enabling robust EB to be established after field cooling from 400 K, while preserving structural integrity. Importantly, EB can be subsequently tuned by voltage, up to a 30% enhancement observed at 100 K alongside an increase in saturation magnetization (up to ≈ 250 emu cm^{-3}). Unlike previous works on similar single-layer nitrides, incorporating an additional ferromagnetic Co layer to form an AFM/ferromagnetic bilayer amplifies the voltage-induced effects. This work highlights the dual role of Co addition to MnN: (i) reducing the thermal requirements for setting EB by lowering T_N, and (ii) enhancing electrical control of EB. These results represent a step forward towards the development of low-power voltage-controlled spintronic devices.

1. Introduction

The growing computational demands of big data, the Internet of Things, and artificial intelligence have led to an exponential increase in energy consumption for information processing and storage [1,2]. This has motivated research towards new energy-efficient hardware, with neuromorphic and spintronic devices at its core. In this context, magneto-ionics (MI), i.e., the voltage-driven control of magnetic properties through ion migration, has emerged as a powerful approach for low-energy, non-thermal manipulation of functional magnetic materials [3–12].

MI materials enable non-volatile modification of key magnetic properties such as saturation magnetization (M_S) [12–17] or anisotropy [7,18]. Notably, MI offers unique opportunities for manipulating antiferromagnetic (AFM) materials with external stimuli, otherwise challenging due to their insensitivity to applied magnetic fields. Namely, in AFM/ferromagnetic (FM) heterostructures, MI can tune the exchange bias (EB) effect [8,19–27], i.e., a shift of the hysteresis loop along the magnetic field axis after field cooling (FC) through the AFM Néel temperature (T_N), which is particularly valuable for spintronic applications [28–32].

In this context, nitrides are a particularly promising avenue for exploration, as the N^{3-} anion exhibits unique bonding characteristics, e.g., it is stable at room temperature (RT) and forms AFM compounds with numerous metals such as Mn, Cr, and Fe [33–36]. Critically, N^{3-} MI systems show better performance over oxygen-based MI analogues [5,14,37–39].

Manganese nitrides stand out among transition metal nitrides through their robust AFM behavior and demonstrated MI efficiency [14,23,40,41]. However, pure MnN has a relatively high T_N, 660 K. Consequently, the FC process to induce EB can lead to phase transformations or a thermally driven N-redistribution, thereby complicating EB control. Doping offers a viable

strategy to modulate T_N in AFM compounds [42,43], yet there is little research in ternary AFM nitrides based on Mn, despite many "new" stable phases have been predicted in systems such as Mn-Co-N [34,44,45]. Consequently, this study explores the AFM and magneto-ionic properties of the ternary nitride $Mn_{1-x}Co_xN$ ($0 < x < 0.24$).

Here, EB is observed in Ta/$Mn_{1-x}Co_xN$(AFM)/Co(FM)//Ta heterostructures using mild FC conditions (T_{FC} = 400 K). This approach minimizes nitrogen interdiffusion and preserves the AFM structure, owing to the reduction of the blocking temperature (T_B) distribution through Co addition. Subsequent voltage actuation enables pronounced modulation of the system's magnetic properties, including EB. While previous works on all-solid-state MI in $Mn_{1-x}Co_xN$ single layers reported small effects due to the overall low magnetization of the films [15], the inclusion of an adjacent FM Co film enhances the magnetic signal, resulting in more significant voltage-induced effects, with potential for realistic applications. The combination of optimized T_B and voltage-driven MI control of EB in the $Mn_{1-x}Co_xN$/Co heterostructures offers a promising platform for tunable spintronic devices.

2. Experimental section

2.1. Sample preparation

The Ta(10 nm)/$Mn_{1-x}Co_xN$(45 nm)/Co(2 nm)/Ta(10 nm) heterostructures were deposited by dc-magnetron sputtering on top of thermally oxidized (285 nm SiO_2) *p*-type Si (001) wafers using a shadow mask that delimited 5 mm × 5 mm squares.

The ternary alloy was deposited at RT from Co (99.99%) and Mn (99.99%) targets at 0.33 Pa in a mixed 1:1 Ar:N_2 atmosphere. The Co content was changed by adjusting the power and geometry while maintaining a constant Mn power (50 W) [15]. The FM Co layer and the Ta seed and top layers were deposited at RT, 3 mTorr, and 50 W from metallic targets in a pure Ar atmosphere.

2.2. Magnetic characterization

Hysteresis loops (100–300 K) were measured using a LakeShore-8600 vibrating sample magnetometer (VSM) with the field parallel to the sample surface. To induce EB, samples were FC inside the VSM from either T_{FC} =675 K, 400 K, or RT down to either RT or 100 K under a 10 kOe in-plane field. All the loops were shown after removing any training effects.

The voltage conditioning (VC) of the samples was performed ex-situ by applying 20 V for 1 h after FC from 400 K. The Ta layers became partially nitrided as they spontaneously attract nitrogen from the $Mn_{1-x}Co_xN$ [23]. Thus, the conductivity of the Ta layers was expected to be much lower than that for pure Ta [46], hindering possible electrostatic screening during gating.

2.3. Structural and compositional characterization

Film composition and homogeneity were quantified through energy-dispersive X-ray spectroscopy. X-ray diffraction (XRD) patterns were obtained using Cu K_α radiation from a Malvern-Panalytical X'Pert3 MRD system and a Rigaku SmartLab diffractometer. X-ray reflectivity scans were obtained using the Rigaku Smartlab. Surface roughness was characterized using the MFP-3D Origin+ Atomic Force Microscope, in tapping mode.

2.4. Neutron scattering

Polarized neutron reflectivity (PNR) experiments were carried out on the POLREF instrument at the ISIS Rutherford Appleton Laboratory [47] for the MnN and the $Co_{15}Mn_{85}N$ samples. The samples were measured at RT under a 10 kOe in-plane field (parallel to the FC direction) in various states: as-grown (AG), FC from 675 or 400 K, and after VC. The incident neutron beam was polarized parallel (+) or antiparallel (−) with respect to the magnetic field. There was no polarization analysis of the scattered neutrons, resulting in R^+ and R^- reflectivities being measured with respect to the wave vector transfer, Q, along the film normal direction. Data were reduced using Mantid data reduction software [48,49], and Refl1D software packages were used for fitting. Error bars for the fitted parameters were determined with a Markov chain Monte Carlo method using the BUMPS software package [50]. The theoretical fits of the reflectivity, depth profile, and the magnetic component (ρ_M) of the scattering length density (SLD) were calculated from the best-fit model chosen for the system. Further discussion

of the fits is available in S.1 in the Supplementary Materials.

3. Results and discussion

3.1. Structural and magnetic characterization

A schematic of the samples is depicted in Fig. 1(a), along with a representation of the VC geometry. XRD patterns of the AG samples exhibit two peaks in the measured angular range (Fig. 1(b)). The more intense peak, marked with a diamond and associated with the ternary layer, progressively shifts from 2θ = 42.6° (θ-MnN) [23,51] to 43.2° as the Co content is increased. This progressive shift is associated with the atomic substitution of Co into MnN [15]. Additionally, this peak broadens and becomes asymmetric with the progressive Co inclusion, suggesting the emergence of a new phase, similar to previous studies [15].

The less intense peak around 2θ = 38° is consistent with tetragonal Ta, Ta_2N, TaN or Ta_2O_5, all with peaks in the 35°–40° range. Although the peak is present in all samples, it is not clearly evident in all XRD patterns, given its low intensity. The intensity of this peak depends on the crystallinity of the Ta[N, O] layer(s) and the relative amount of each phase,

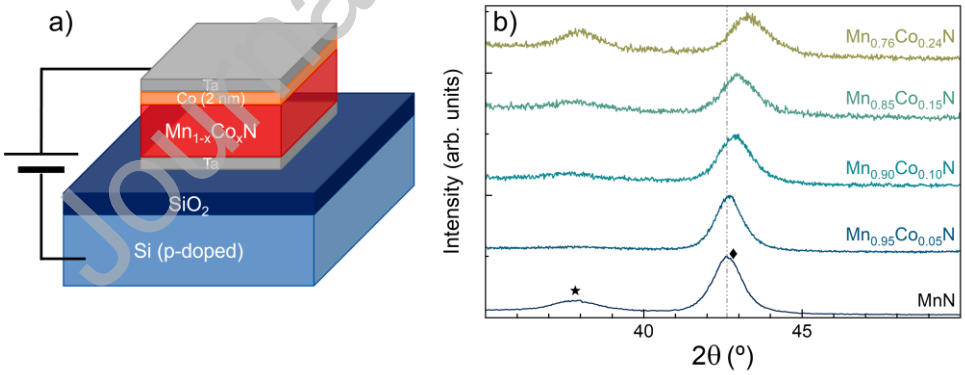

Fig. 1. (a) Schematic of the heterostructures with the gating configuration. (b) XRD patterns for the AG samples up to x = 0.24. *-TaN_x; ♦-$Mn_{1-x}Co_xN$.

which depends on the structure of the underlying $Mn_{1-x}Co_xN$ layer.

Fig. 2(a–d) shows in-plane hysteresis loops for all samples in the AG state and after FC

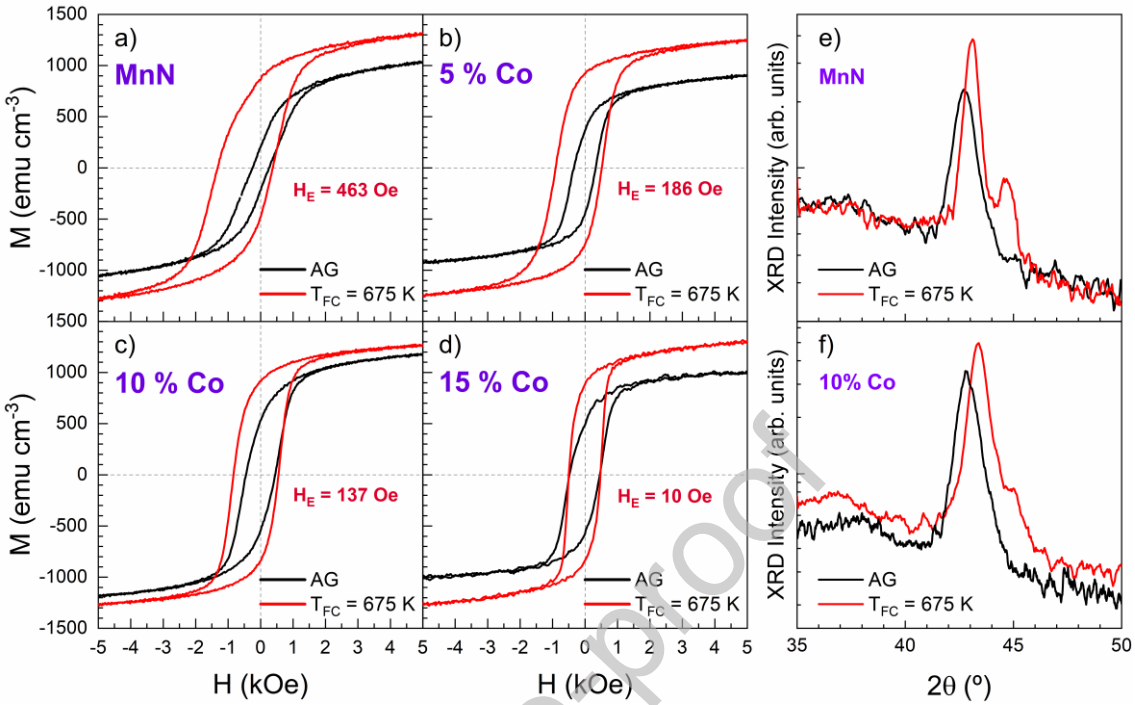

Fig. 2. RT hysteresis loops for the (a) 0%, (b) 5%, (c) 10%, and (d) 15% at. Co samples in the AG (black) and after FC-675 K states (red). (e and f) XRD patterns for the MnN and $x = 0.10$ samples before and after FC.

under 10 kOe from T_{FC} = 675 K to RT. In the AG state, the hysteresis loops are centered (i.e., no EB) for all compositions and exhibit lower saturation magnetization (M_S = 980–1200 emu cm^{-3}) than that expected for Co ($M_{S,\,Co} \approx 1422$ emu cm^{-3}), likely due to Co nitridation during growth. In contrast, after FC from 675 K, M_S increases up to ≈ 1400 emu cm^{-3}, and the loops for the samples with $x < 0.15$ display significant EB [28,32]. This increase is associated with a thermally-mediated removal of the nitrogen incorporated in the FM Co layer during growth towards Ta, forming TaN_x [23,52]. The EB field (H_E) decreases with the Co content in the nitride layer, starting from H_E = 463 Oe in MnN and reaching 137 Oe for x = 0.10. For compositions with higher Co content (x = 0.15, 0.24), H_E becomes negligible (≤ 10 Oe). The large H_E of the MnN sample is expected since it is a known AFM material with T_N = 660 K [35,41,53]. The decrease in H_E as Co is incorporated stems from multiple factors, such as

changes in the AFM characteristics (e.g., T_N or anisotropy), differences in the nitrogen migration due to the presence of Co [23,24,54] or the interface roughness [29,55,56] (S.2 in the Supplementary Materials).

Interestingly, the XRD patterns of the FC samples (Fig. 2(e and f)) reveal considerable

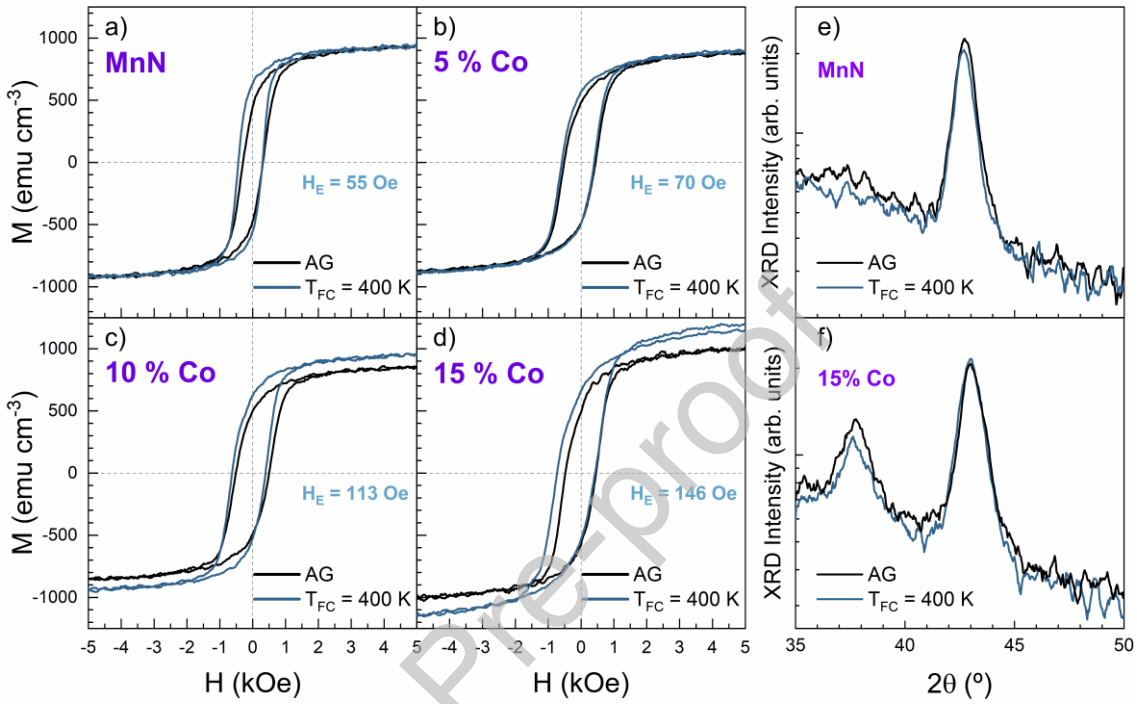

Fig. 3. RT hysteresis loops for the (a) 0%, (b) 5%, (c) 10%, and (d) 15% at. Co samples in the AG (black) and after FC-400 K states (blue). (e and f) XRD patterns for the MnN and $x = 0.15$ samples before and after FC.

structural changes in the $Mn_{1-x}Co_xN$ layer. The ternary peak becomes sharper and shifts by ≈ 0.5° for both $x = 0$ and 0.10, indicating thermally-driven nitrogen redistribution and increased crystallite size, further confirmed by field-free annealing (S.2 in the Supplementary Materials). Additionally, after FC, a clear peak appears between $2\theta = 44.5°–45°$ for both samples. This effect is related to the loss of nitrogen and formation of tetragonal η-Mn_3N_2 during heating [23,57]. These substantial structural changes lead to irreversibility and strong unpredictability in the magnetic properties, as demonstrated by the unequal values of H_E obtained when FC the same sample in opposite fields (S.3 in the Supplementary Materials). Consequently, after FC-675 K, the EB properties arise from a convolution of multiple magnetic and structural effects

that inevitably influence magnetism. As a result, the capacity to predictably tune H_E by adjusting a single magnetic parameter is compromised. Finally, the lack of EB in the $Mn_{0.76}Co_{0.24}N$ sample after FC-675 K indicates that this sample might not be AFM at RT.

To avoid the structural changes induced by the high-temperature FC, a milder FC from T_{FC} = 400 K under 10 kOe was carried out. In contrast to the FC-675 K case, the EB progressively increases from H_E = 55 Oe in the x = 0 sample to a maximum of H_E = 146 Oe in the x = 0.15 sample (Fig. 3(a–d)). Note that with these FC conditions, the sample with x = 0.24 presents H_E = 30 Oe. In addition, M_S after FC-400 K remains similar to that in the AG state, indicating low N mobility at 400 K. Remarkably, the XRD results suggest that the crystalline structure of the samples was retained after the heat treatment (Fig. 3(e and f); S.2 in the Supplementary Materials).

Fig. 4 summarizes the dependence of H_E and the H_C on the Co percentage in the ternary

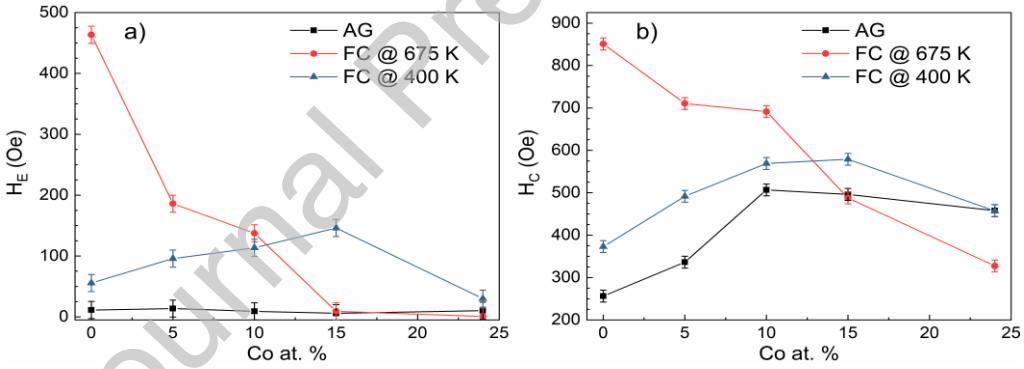

Fig. 4. Summary of the (a) H_E and (b) coercivity (H_C) dependence with the Co at.% at RT in the AG (black squares), FC-675 K (red circles) and FC-400 K (blue triangles) states.

layer at RT for the AG, FC-675 K, and FC-400 K states. While H_E is negligible for the AG samples, its trend in the FC-675 K and FC-400 K states is remarkably different. On the other hand, H_C steadily increases with the Co content from 256 Oe (x = 0) to 507 Oe (x = 0.10) in the AG state and from 373 Oe (x = 0) to 569 Oe (x = 0.10) in the FC-400 K state. Finally, H_C decreases to 458 Oe in both states for the x = 0.24 sample. Conversely, the trend in H_C for the FC-675 K state is a continuous decrease, from H_C = 851 Oe for x = 0 to H_C = 327 Oe for x =

0.24.

These results evidence several unexpected trends. Firstly, EB is observed in MnN at RT after FC-400 K, even with $T_N >> T_{FC}$. Although the T_N of MnN is 660 K, the film presents a distribution of blocking temperatures (ΔT_B) that spans below 400 K, an effect observed in similar heterostructures [58–61]. Thus, while FC from 675 K activates most of the AFM grains (leading to a large H_E), FC from 400 K already activates some of the AFM grains, resulting in a smaller H_E [60,62] (S.3 in the Supplementary Materials). Secondly, the increase of H_E up to $x = 0.15$ after FC-400 K is also related to ΔT_B, since a given T_{FC} can activate different amounts of AFM grains, leading to different H_E values (S.3 in the Supplementary Materials) [32,63]. In addition, the progressive increase of H_C of the AG samples with increasing Co content suggests that some coupling is already taking place at RT. Note that given the random distribution of AFM grains, if no FC is carried out, the exchange coupling between the AFM and FM layers should lead to H_C enhancement with increasing Co concentration, without H_E [32].

These results indicate that the samples have different T_N (T_B) and a broad ΔT_B, where T_B progressively lowers with increasing Co content. This effect is pivotal to allow moderate EB while retaining the crystalline phase after the mild annealing. For example, the evaluation of the sample with $x = 0.15$ shows that the average T_B is about 350 K with a large distribution (S.3 in the Supplementary Materials), i.e., considerably lower than $T_{N,\,MnN}$ [35,41]. Importantly, in contrast to FC-675 K, FC-400 K in a negative cooling field leads to $-|H_E|$, as expected, indicating that the observed effects are purely magnetic.

To further assess the decrease in T_B, hysteresis loops were recorded below RT in the AG and FC-400 K states (Fig. 5 and S.4 in the Supplementary Materials). Cooling from 300 K was conducted under a magnetic field. As expected, H_C and H_E increase as the temperature is lowered in both states. Interestingly, while H_C and H_E for $x = 0.15$ change considerably when FC is from 300 K (AG) and FC from 400 K, the changes between the AG and FC-400 K states

for x = 0.24 are less evident. This suggests that T_B and its distribution for x = 0.24 lie below RT (i.e., FM-AFM exchange coupling is mainly induced below RT).

As can be seen in Fig. 6, in the AG state (Fig. 6(a and d)), the trend in H_C with Co addition

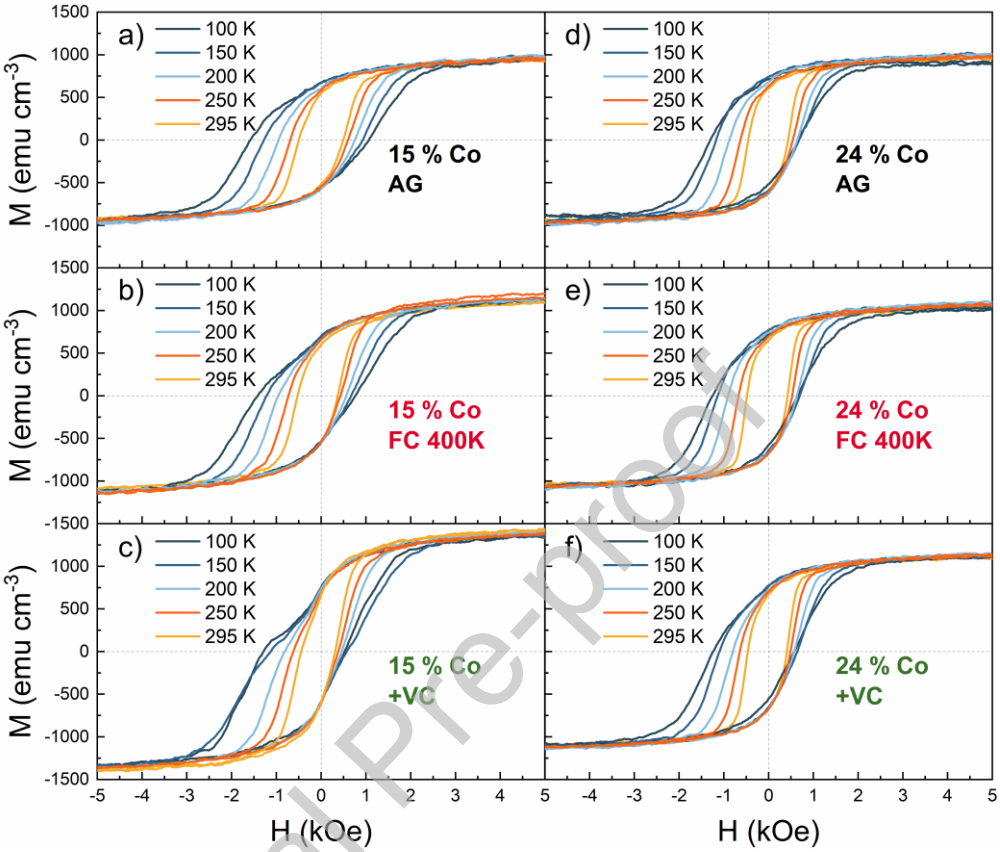

Fig. 5. Hysteresis loops from 100 K to RT for the 15% at. Co sample (a–c) and the 24% at. Co sample (d–f) in the AG (a and d), FC-400 K (b and e) and VC (c and f) states.

is similar at all measured temperatures, following an analogous behavior as that observed at RT. While no EB is observed at RT, samples exhibit an H_E proportional to the Co content after FC down from RT to 100 K, reaching H_E = 315 Oe for x = 0.24 at 100 K. The presence of EB below 300 K in some of the samples after FC from RT further confirms the shift of ΔT_B towards lower temperatures with the addition of Co.

In the FC-400 K state (Fig. 6(b and e)), EB is already observed at RT for all samples, and it follows a similar trend to the AG state with decreasing temperature. The matching H_E values for x = 0.24 in the AG and FC-400 K states below 250 K indicate that ΔT_B resides entirely below RT. Additionally, the H_C values for the samples with x = 0 and 0.05 are almost double

compared to the AG state, contrary to the H_C values for compositions with $x > 0.10$, which remain similar after the FC treatment.

3.2. Voltage-induced effects on magnetic properties

Subsequently, the effect of VC (+20 V for 1 h) on the FC-400 K samples was investigated. The H_C and H_E values for the loops in Fig. 5(c and f) and S.4 in the Supplementary Materials are summarized in Fig. 6(c and f). After voltage is applied, two magnetic contributions become evident in the sample with $x = 0.15$ (note the kink in Fig. 5(c)), especially at lower temperatures. Similar effects are found for the $x = 0.10$ sample and are less noticeable for $x = 0.24$. The origin of this new soft, unbiased magnetic phase is later discussed in detail.

Hysteresis loops exhibiting a post-VC kink were deconvoluted into a "soft" and a "hard" contribution (S.5 in the Supplementary Materials) to obtain the H_C and H_E values from the "hard" contribution [64,65]. In particular, the two samples most affected by the VC ($x = 0.10$ and 0.15) are the ones that exhibit most clearly this distinct kink in their hysteresis loop, along with the largest increase in M_S post-VC treatment at RT compared to the FC-400 K state.

Additionally, more systematic MI modulation experiments are presented in S.6 in the Supplementary Materials. From the results, the 20 V-1h gating condition was chosen as the best balance between maximizing both MI effects and energy efficiency.

Remarkably, the VC effects are strongly sample-dependent, as shown in Fig. 6. For instance, in the MnN sample, both H_C and H_E decrease after the VC treatment at all measured temperatures. In contrast, samples containing Co exhibit distinct behaviors at low temperatures compared to near RT. For $x = 0.10$, the difference in H_E is minor across the whole T range, despite H_C increasing by around 8%. Conversely, for $x = 0.15$, despite both parameters decreasing at RT, they increase up to 30% below 150 K. Finally, the sample with 24at.% Co is not significantly affected by the VC above 150 K, but H_E increases modestly from 318 to 346 Oe at 100 K between the FC-400 K and VC states. The observed changes are highly reversible

upon application of a voltage with the opposite polarity (S.7 in the Supplementary Materials).

Two mechanisms can be considered to explain the VC-induced effects. The first is the removal of residual

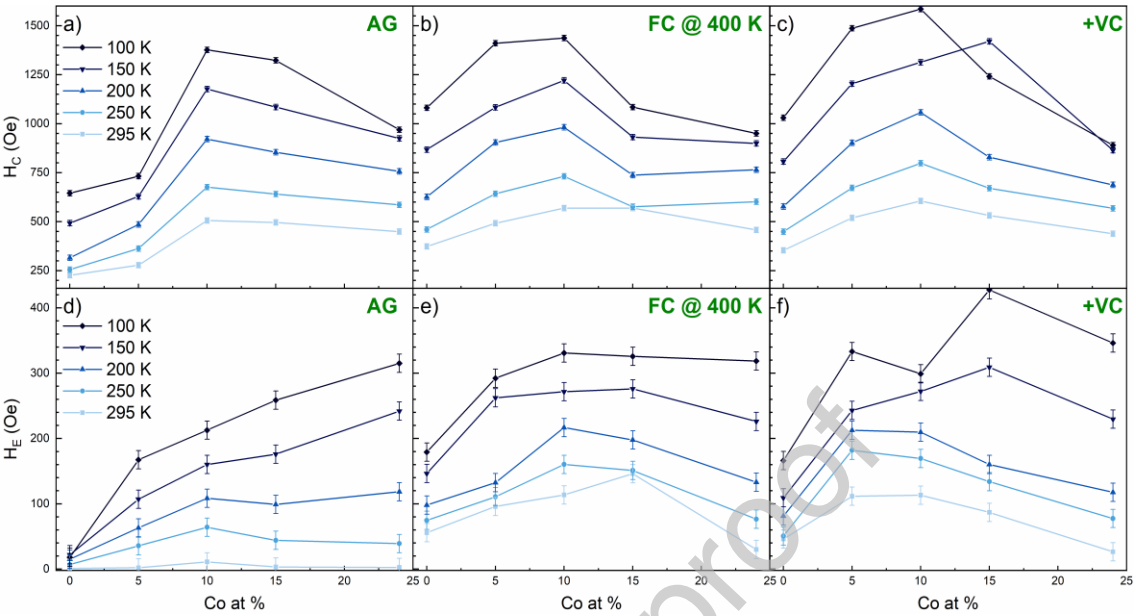

Fig. 6. Summary of (a–c) H_C and (d–f) H_E dependence with the Co at.% in the (a and d) AG, (b and e) FC-400 K, and (c and f) VC states. The dependences are shown for all temperatures measured, from 100 K to RT, from dark blue to light blue, respectively.

N from the Co FM layer (incorporated during the film growth) towards Ta, increasing M_S while decreasing H_E, since $H_E \propto M_S^{-1}$. Alternatively, gating can trigger N displacement out of the ternary layer. In this case, the increase in M_S would arise from the formation of less nitridated phases of $(Mn, Co)_xN_y$ near the interface with the FM Co, similarly to the gating effects in $Co_xMn_{1-x}N$ single films [15]. The new phases would be uncoupled from the AFM at RT, effectively reducing H_E. However, upon cooling down to 100 K, these unpinned clusters could couple to the AFM grains with T_B < RT, thereby increasing the observed H_E below RT. In both scenarios, the newly formed magnetic phases would be responsible for the kink observed after VC. Nevertheless, determining the exact mechanism at this stage remains challenging.

3.3. PNR analysis

PNR was performed on a Ta/$Mn_{0.85}Co_{0.15}N$/Co/Ta heterostructure in the AG, FC-400 K, and VC states to investigate the nitrogen redistribution. This technique is well-suited for detecting ionic migration due to the large nuclear SLD (ρ) contrast between Mn and MnN [23,24].

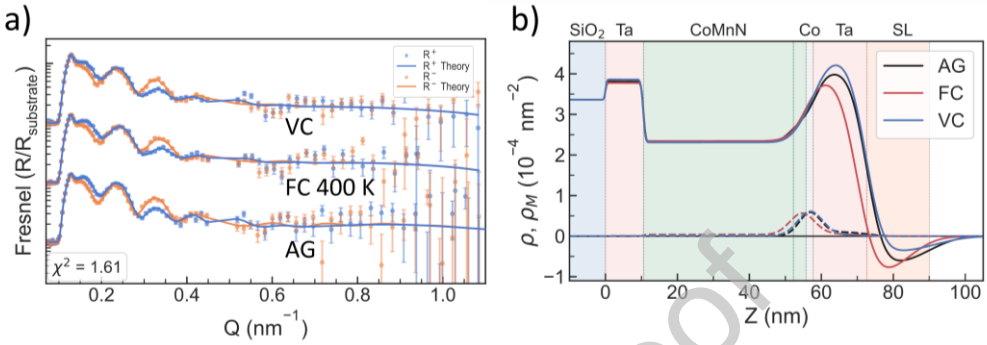

Fig. 7. (a) Data (symbols with error bars) and theoretical fits (solid lines) for PNR performed on Ta/$Mn_{0.85}Co_{0.15}N$/Co/Ta samples in the AG, FC-400 K, and VC states. Curves offset for visual clarity; error bars represent standard deviation. (b) SLD depth profiles for the sample states of the Ta/$Mn_{0.85}Co_{0.15}N$/Co/Ta heterostructure. ρ is shown in solid lines and ρ_M in dashed lines. Background regions indicate the approximate AG layer locations, labeled at the top of the figure.

Fig. 7(a) shows the R^+ and R^- reflectivities for the sample with x = 0.15 in the AG, FC-400 K, and VC states. Small changes can be seen in the reflectivity between the states, notably in the Q ranges of 0.15–0.20 and 0.30–0.35 nm^{-1}. The change between the AG and FC-400 K states is insignificant compared to the large PNR differences previously reported in MnN-based systems annealed at 700 K [23,66]. For comparison, the pure MnN was studied in the AG, FC-400 K, and FC-675 K states (S.1 in the Supplementary Materials). While FC-400 K causes no significant changes, FC-675 K induced substantial reflectivity shifts, consistent with nitrogen loss and thickness variations previously observed in Ta/MnN/CoFe/Ta heterostructures [23,66]. This confirms that T_{FC} = 400 K is below the threshold for inducing significant thermal ionic migration.

Fig. 7(b) illustrates the depth profile of ρ (solid lines) and the magnetic component (ρ_M, dashed lines) of the SLD for the best-fit model (details in S.1 in the Supplementary Materials). The $Mn_{0.85}Co_{0.15}N$ layer was split into two sub-layers, one representing the bulk of the ternary layer and a transition layer at the interface between $Mn_{0.85}Co_{0.15}N$ and Co. Although differences in the depth profile of ρ among the three states are noticeable, the 95% confidence interval (CI) overlap indicates they are statistically insignificant.

While the fit values for ρ_M of the bulk $Mn_{0.85}Co_{0.15}N$ layer are nearly zero, the transition layer exhibits a finite magnetization that increases after the FC-400 K and the VC treatments (S.1 in the Supplementary Materials). Remarkably, the sum of the transition layer and Co layer magnetization yields a moment comparable to magnetometry results for the AG and FC-400 K states (Table 1). Note that the M_S values in Table 1 are normalized by area to exclude the uncertainty of the thickness determined through PNR. For the VC state, the magnetometry result lies within the 95% CI of the PNR-computed moment. These observations indicate that the magnetic changes originate in the interface region between the FM Co and transition layers.

Table 1

Moment per sample area values and 95% CI.

State	Calc. method	Moment ($\times 10^{-6}$ emu cm^{-2})	Moment 95% CI ($\times 10^{-6}$ emu cm^{-2})
AG	Magnetometry	211.6	–
	PNR	213.8	154.2–273.4
FC-400 K	Magnetometry	240.0	–
	PNR	248.6	177.5–319.6
VC	Magnetometry	294.0	–
	PNR	221.3	146.2–296.3

Overall, the PNR results indicate a limited nitrogen migration between the three states, which still translates into significant magnetic restructuring. The VC-induced moment increase

is localized at the $Mn_{0.85}Co_{0.15}N$/Co interface, similar to that observed in single $Co_xMn_{1-x}N$ films [15]. The absence of a substantial moment increase in the MnN sample (S.6 in the Supplementary Materials) rules out Co denitridation, i.e., one of the two previously proposed mechanisms, as it would affect all compositions evenly (resembling the thermally induced denitridation after FC-675 K). Instead, N^{3-} depletion at the FM/AFM interface, eventually forming a magnetic phase, would degrade the interfacial quality, consistent with the observed overall reduction in H_E and H_C at RT.

The improved VC-controlled tuning of EB for the sample with x = 0.15 stems from the synergistic combination of reduced T_N/T_B and higher N mobility due to the Co incorporation in the $Mn_{1-x}Co_xN$ layer [14]. Notably, while VC modulation of EB has been observed in single $Mn_{1-x}Co_xN$ layers, their extremely reduced magnetization (10–20 emu cm^{-3}) [15] limits their potential practical use. In contrast, the addition of the FM Co layer has a crucial three-fold effect: (i) considerably increases the measurable M_S of the system; (ii) enables observation of the VC-induced EB tuning at higher temperatures; and (iii) VC increases EB for some compositions, in comparison to Co-rich $Mn_{1-x}Co_xN$ layers that have been previously reported [15].

4. Conclusions

This study demonstrates that moderate cobalt addition to MnN ($Mn_{1-x}Co_xN$) lowers the T_B distribution of the AFM phase, enabling EB to be established via milder FC conditions (T_{FC} = 400 K). This allows for engineering the AFM properties, reducing the required thermal energy for establishing EB, preserving structural and interfacial integrity at the expense of somewhat reduced H_E values.

Additionally, we demonstrate reversible voltage-driven control of the EB. VC leads to an increase in M_S alongside a decrease in H_E at RT. However, an increase of H_E up to ~30% can be obtained below RT for the 15at.% Co sample. These changes are attributed to interfacial formation of less-nitridated phases near the $Mn_{0.85}Co_{0.15}N$/Co interface (e.g., $(Mn_{1-x}Co_x)_4N$).

These findings show that $Mn_{1-x}Co_xN$ heterostructures achieve dual tunability: (i) thermal activation with reduced energy usage and (ii) enhanced magneto-ionic modulation of M_S and

H_E. Furthermore, the electric-field tailoring of M_S and H_E surpasses in modulation magnitude prior reports in similar systems with the absence of the Co FM adjacent layer, owing to the intrinsically enhanced magnetic signal. This sets $Mn_{1-x}Co_xN$ heterostructures compelling candidates for low-power magneto-ionic devices. Their controllability both during deposition (composition) and post-deposition (MI) unlocks appealing pathways for engineering low-power spintronic and memory applications without necessarily having to grow various samples to introduce changes in the resulting magnetic properties.

Our results constitute a proof-of-principle demonstration, showing a practical method to tune T_N/T_B in ternary nitride systems, which allows for sizeable magneto-ionic effects. However, for practical applications, the Co content, field-cooling conditions, and gating parameters must be optimized to ensure compatibility with device performance.

Finally, it is important to highlight that although mechanisms based on electrical currents to manipulate magnetic properties (e.g., via spin-orbit coupling [67,68]) can be very fast and effective, they are not energetically efficient, particularly since electric currents lead to Joule heating. Consequently, approaches based on electric fields (like MI), which can be potentially energetically more efficient, are being developed. Thus, although MI has certain limitations, like speed, it allows for more efficient magnetic computing architectures, especially when using this effect in the framework of neuromorphic computing [6].

Acknowledgements

Financial support from the European Research Council (2021-ERC-Adv Grant N° 101054687 and 2024-ERC-PoC Grant N° 101204328), the Spanish Government (PID2024-156385OB-I00, PDC2021-121276-C31 and the MCIN/AEI/10.13039/501100011033 & "NextGenerationEU/PRTR" grant CNS2022-135230) and the Generalitat de Catalunya (2021-SGR-00651) is acknowledged. Views and opinions expressed are those of the authors. Neither the EU nor the granting authority can be held responsible for them. Work at Georgetown

University was supported by the US NSF (ECCS-2429995) and AFOSR DEPSCoR (FA9550-23-1-0497). This study utilized a Magnetic Property Measurements System (MPMS3), acquired with support from the US NSF-MRI (DMR-1828420). Enric Menéndez is a Serra Húnter Fellow. ICN2 is funded by the CERCA programme/Generalitat de Catalunya and supported by the CEX2021-001214-S grant funded by MCIN/AEI/10.13039/501100011033. We gratefully acknowledge the STFC for access to neutron beamtime at the ISIS neutron and muon (RB2410415). NIST work was funded solely by the United States Government.

References

[1] N. Jones, Nature 561 (2018) 163–166.

[2] S. Chen, Nature (2025). DOI: 10.1038/d41586-025-01113-z.

[3] C. Navarro-Senent, A. Quintana, E. Menéndez, E. Pellicer, J. Sort, APL Mater. 7 (2019) 030701.

[4] S. Fusil, V. Garcia, A. Barthélémy, M. Bibes, Annu. Rev. Mater. Res. 44 (2014) 91–116.

[5] J. De Rojas, A. Quintana, G. Rius, C. Stefani, N. Domingo, J.L. Costa-Krämer, E. Menéndez, J. Sort, Appl. Phys. Lett. 120 (2022) 070501.

[6] P. Monalisha, M. Ameziane, I. Spasojevic, E. Pellicer, R. Mansell, E. Menéndez, S. van Dijken, J. Sort, Small Sci. 4 (2024) 2400133.

[7] U. Bauer, L. Yao, A.J. Tan, P. Agrawal, S. Emori, H.L. Tuller, S. Van Dijken, G.S.D. Beach, Nat. Mater. 14 (2015) 174–181.

[8] D.A. Gilbert, J. Olamit, R.K. Dumas, B.J. Kirby, A.J. Grutter, B.B. Maranville, E. Arenholz, J.A. Borchers, K. Liu, Nat. Commun. 7 (2016) 11050.

[9] D.A. Gilbert, A.J. Grutter, E. Arenholz, K. Liu, B.J. Kirby, J.A. Borchers, B.B. Maranville, Nat. Commun. 7 (2016) 12264.

[10] C. Leighton, Nat. Mater. 18 (2019) 13–18.

[11] K. Duschek, D. Pohl, S. Fähler, K. Nielsch, K. Leistner, APL Mater. 4 (2016) 032301.

[12] A.J. Tan, M. Huang, C.O. Avci, F. Büttner, M. Mann, W. Hu, C. Mazzoli, S. Wilkins, H.L. Tuller, G.S.D. Beach, Nat. Mater. 18 (2018) 35–41.

[13] J. de Rojas, A. Quintana, A. Lopeandía, J. Salguero, B. Muñiz, F. Ibrahim, M. Chshiev, A. Nicolenco, M.O. Liedke, M. Butterling, A. Wagner, V. Sireus, L. Abad, C.J. Jensen, K. Liu, J. Nogués, J.L. Costa-Krämer, E. Menéndez, J. Sort, Nat. Commun. 11 (2020) 5871.

[14] Z. Tan, S. Martins, M. Escobar, J. De Rojas, F. Ibrahim, M. Chshiev, A. Quintana, A. Lopeandia, J.L. Costa-Krämer, E. Menéndez, J. Sort, ACS Appl. Mater. Interfaces 14 (2022) 44581–44590.

[15] N. López-Pintó, C.J. Jensen, Z. Chen, Z. Tan, Z. Ma, M.O. Liedke, M. Butterling, A. Wagner, J. Herrero-Martín, E. Menéndez, J. Nogués, K. Liu, J. Sort, Adv. Funct. Mater. 34 (2024) 2404487.

[16] S. Robbennolt, E. Menéndez, A. Quintana, A. Gómez, S. Auffret, V. Baltz, E. Pellicer, J. Sort, Sci. Rep. 9 (2019) 10804.

[17] A. Quintana, E. Menéndez, M.O. Liedke, M. Butterling, A. Wagner, V. Sireus, P. Torruella, S. Estradé, F. Peiró, J. Dendooven, C. Detavernier, P.D. Murray, D.A. Gilbert, K. Liu, E. Pellicer, J. Nogues, J. Sort, ACS Nano 12 (2018) 10291–10300.

[18] B. Bednarz, M.A. Syskaki, R. Pachat, L. Prädel, M. Wortmann, T. Kuschel, S. Ono, M. Kläui, L. Herrera Diez, G. Jakob, Appl. Phys. Lett. 124 (2024) 232403.

[19] P.D. Murray, C.J. Jensen, A. Quintana, J. Zhang, X. Zhang, A.J. Grutter, B.J. Kirby, K. Liu, ACS Appl. Mater. Interfaces 13 (2021) 38916–38922.

[20] C.J. Jensen, A. Quintana, M. Sall, L.H. Diez, J. Zhang, X. Zhang, D. Ravelosona, K. Liu, J. Magn. Magn. Mater. 540 (2021) 168479.

[21] J. Zehner, D. Wolf, M.U. Hasan, M. Huang, D. Bono, K. Nielsch, K. Leistner, G.S.D. Beach, Phys. Rev. Mater. 5 (2021) L061401.

[22] Y. Luo, S. Liu, Y. Li, Z. Wang, J. Zhang, L. Zheng, Crystals 15 (2025) 77.

[23] C.J. Jensen, A. Quintana, P. Quarterman, A.J. Grutter, P.P. Balakrishnan, H. Zhang, A.V. Davydov, X. Zhang, K. Liu, ACS Nano 17 (2023) 6745–6753.

[24] Z. Chen, C.J. Jensen, C. Liu, Y. Liu, C.J. Kinane, A.J. Caruana, A.J. Grutter, J.A. Borchers, X. Zhang, K. Liu, ACS Nano 19 (2025) 20072–20083.

[25] M.U. Hasan, A.E. Kossak, G.S.D. Beach, Nat. Commun. 14 (2023) 8510.

[26] M. Gößler, J. Zehner, R. Huhnstock, F. Röder, R. Ehrler, O. Hellwig, A. Ehresmann, K. Leistner, ACS Appl. Mater. Interfaces 17 (2025) 49671–49682.

[27] G.V. de Oliveira Silva, L. Ghosh, R. Islam, C.I.L. de Araujo, G.X. Miao, ACS Nano 19 (2025) 20799–20807.

[28] J. Nogués, J. Sort, V. Langlais, V. Skumryev, S. Suriñach, J.S. Muñoz, M.D. Baró, Phys. Rep. 422 (2005) 65–117.

[29] T. Blachowicz, A. Ehrmann, Coatings 11 (2021) 122.

[30] W. Zhang, K.M. Krishnan, Mater. Sci. Eng. R-Rep. 105 (2016) 1–20.

[31] R. Gupta, R.K. Kotnala, J. Mater. Sci. 57 (2022) 12710–12737.

[32] J. Nogués, I.K. Schuller, J. Magn. Magn. Mater. 192 (1999) 203–232.

[33] J.M.D. Coey, P.A.I. Smith, J. Magn. Magn. Mater. 200 (1999) 405–424.

[34] W. Sun, C.J. Bartel, E. Arca, S.R. Bauers, B. Matthews, B. Orvañanos, B.R. Chen, M.F. Toney, L.T. Schelhas, W. Tumas, J. Tate, A. Zakutayev, S. Lany, A.M. Holder, G. Ceder, Nat. Mater. 18 (2019) 732–739.

[35] N.A. Gokcen, Alloy Phase Diagr. 11 (1990) 33–42.

[36] Z. You, M.K. Paek, I.H. Jung, J. Phase Equilib. Diffus. 39 (2018) 650–677.

[37] Z. Tan, J. de Rojas, S. Martins, A. Lopeandia, A. Quintana, M. Cialone, J. Herrero-Martín, J. Meersschaut, A. Vantomme, J.L. Costa-Krämer, J. Sort, E. Menéndez, Mater. Horiz. 10 (2022) 88–96.

[38] J. De Rojas, J. Salguero, F. Ibrahim, M. Chshiev, A. Quintana, A. Lopeandia, M.O. Liedke, M. Butterling, E. Hirschmann, A. Wagner, L. Abad, J.L. Costa-Krämer, E. Menéndez, J. Sort, ACS Appl. Mater. Interfaces 13 (2021) 30826–30834.

[39] Z. Ma, P. Monalisha, Z. Tan, E. Pellicer, M.O. Liedke, M. Butterling, A.G. Attallah, E. Hirschmann, A. Wagner, F. Ibrahim, M. Chshiev, E. Menéndez, J. Sort, J. Materiomics 10 (2024) 870–879.

[40] A. Leineweber, R. Niewa, H. Jacobs, W. Kockelmann, J. Mater. Chem. 10 (2000) 2827–2834.

[41] M. Tabuchi, M. Takahashi, F. Kanamaru, J. Alloys Compd. 210 (1994) 143–148.

[42] M.J. Carey, A.E. Berkowitz, Appl. Phys. Lett. 60 (1992) 3060–3062.

[43] H. Shi, Z. Liu, D. Lederman, Phys. Rev. B 72 (2005) 224417.

[44] S. Dugu, R.W. Smaha, S. Quadir, A. Treglia, J. Martin, S. O'Donnell, S. Mahatara, G. Teeter, S. Lany, J.R. Neilson, S.R. Bauers, Phys. Rev. Mater. 8 (2024) 104411.

[45] H. Mitarai, T. Komori, T. Hirose, K. Ito, S. Ghosh, S. Honda, K. Toko, L. Vila, J.P. Attané, K. Amemiya, T. Suemasu, Phys. Rev. Mater. 4 (2020) 094401.

[46] D. Kim, H. Lee, D. Kim, Y. Kim, J. Cryst. Growth 283 (2005) 404–408.

[47] N. López-Pintó, J. Nogués, J. Sort, K. Liu, Z. Chen, C. Kinane, J. Borchers, C.J. Jensen, A.J. Grutter, Enhanced Nitrogen-Based Magneto-Ionic Manipulation of Exchange Bias in Co/CoMnN Heterostructures [dataset], 2024. https://doi.org/10.5286/ISIS.E.RB2410415-2.

[48] O. Arnold, J.C. Bilheux, J.M. Borreguero, A. Buts, S.I. Campbell, L. Chapon, M. Doucet, N. Draper, R. Ferraz Leal, M.A. Gigg, V.E. Lynch, A. Markvardsen, D.J. Mikkelson, R.L. Mikkelson, R. Miller, K. Palmen, P. Parker, G. Passos, T.G. Perring, P.F. Peterson, S. Ren, M.A. Reuter, A.T. Savici, J.W. Taylor, R.J. Taylor, R. Tolchenov, W. Zhou, J. Zikovsky, Nucl. Instrum. Methods Phys. Res. A 764 (2014) 156–166.

[49] O. Arnold, Mantid Project. Mantid: Manipulation and Analysis Toolkit for Instrument Data (Version 6.8) [software], 2022. https://dx.doi.org/10.5286/SOFTWARE/MANTID6.8.

[50] P.A. Kienzle, B. Maranville, S. Prescott, S. Wu, A.J. Caruana, M. Doucet, A. Detiste, A. McCluskey, A. Nelson, D.P. Hoogerheide, A.F. Ahamed, Bumps (Version 0.9. 3) Refl1D: Reflectometry Modeling [software], University of Maryland, 2024.

[51] P. Zilske, D. Graulich, M. Dunz, M. Meinert, Appl. Phys. Lett. 110 (2017) 192402.

[52] A.D. Mah, N.L. Gellert, J. Am. Chem. Soc. 78 (1956) 3261–3263.

[53] K. Suzuki, Y. Yamaguchi, T. Kaneko, H. Yoshida, Y. Obi, H. Fujimori, H. Morita, J. Phys. Soc. Jpn. 70 (2001) 1084–1089.

[54] Z. Chen, C.J. Jensen, C. Liu, X. Zhang, K. Liu, Appl. Phys. Lett. 123 (2023) 082403.

[55] J. Nogués, D. Lederman, T.J. Moran, I.K. Schuller, K.V. Rao, Appl. Phys. Lett. 68 (1995) 3186–3188.

[56] J. Nogués, T.J. Moran, D. Lederman, I.K. Schuller, K.V. Rao, Phys. Rev. B 59 (1999) 6984–6993.

[57] M. Dunz, J. Schmalhorst, M. Meinert, AIP Adv. 8 (2018) 056304.

[58] M. Meinert, B. Büker, D. Graulich, M. Dunz, Phys. Rev. B 92 (2015) 144408.

[59] J. Sinclair, A. Hirohata, G. Vallejo-Fernandez, M. Meinert, K. O'Grady, J. Magn. Magn. Mater. 476 (2019) 278–283.

[60] K. O'Grady, J. Sinclair, K. Elphick, R. Carpenter, G. Vallejo-Fernandez, M.I.J. Probert, A. Hirohata, J. Appl. Phys. 128 (2020) 040901.

[61] P.J. van der Zaag, Y. Ijiri, J.A. Borchers, L.F. Feiner, R.M. Wolf, J.M. Gaines, R.W. Erwin, M.A. Verheijen, Phys. Rev. Lett. 84 (2000) 6102–6105.

[62] S. Brück, J. Sort, V. Baltz, S. Suriñach, J.S. Muñoz, B. Dieny, M.D. Baró, J. Nogués, Adv. Mater. 17 (2005) 2978–2983.

[63] S. Soeya, T. Imagawa, K. Mitsuoka, S. Narishige, J. Appl. Phys. 76 (1994) 5356–5360.

[64] P. Maltoni, R. López-Martín, E.H. Sánchez, P.S. Normile, M. Vasilakaki, S.S. Lee, B.S. Burgos, E.A.L. del Castillo, D. Peddis, C. Binns, K. Trohidou, R. Mathieu, J. Nogués, J.A. De Toro, Adv. Compos. Hybrid Mater. 7 (2024) 182.

[65] D.A. Gilbert, P.D. Murray, J. De Rojas, R.K. Dumas, J.E. Davies, K. Liu, Sci. Rep. 11 (2021) 4018.

[66] P. Quarterman, Y. Fan, Z. Chen, C.J. Jensen, R.V. Chopdekar, D.A. Gilbert, M.E. Holtz, M.D. Stiles, J.A. Borchers, K. Liu, L. Liu, A.J. Grutter, Phys. Rev. Mater. 6 (2022) 094418.

[67] X.H. Liu, K.W. Edmonds, Z.P. Zhou, K.Y. Wang, Phys. Rev. Appl. 13 (2020) 014059.

[68] P.H. Lin, B.Y. Yang, P.C. Chen, K.F. Huang, H.H. Lin, CH. Lai, Nat. Mater. 18 (2019) 335–341.

Graphical abstract

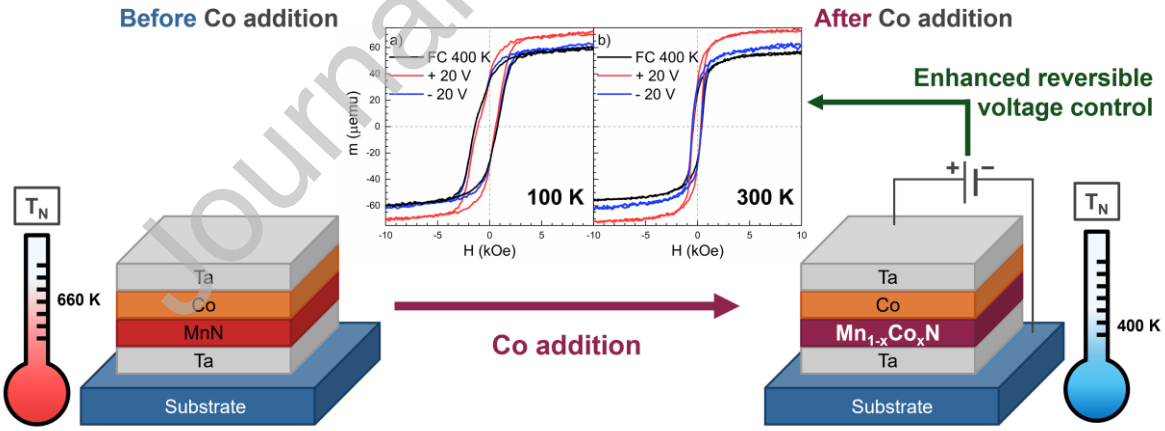

Declaration of Interest Statement

☒ The authors declare that they have no known competing financial interests or personal relationships that could have appeared to influence the work reported in this paper.

☐ The author is an Editorial Board Member/Editor-in-Chief/Associate Editor/Guest Editor for this journal and was not involved in the editorial review or the decision to publish this article.

☐ The authors declare the following financial interests/personal relationships which may be considered as potential competing interests: